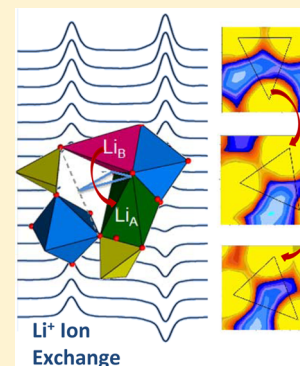


# An Improved Understanding of Li<sup>+</sup> Hopping Pathways and Rates in Li<sub>3</sub>Fe<sub>2</sub>(PO<sub>4</sub>)<sub>3</sub> Using Selective Inversion <sup>6</sup>Li NMR Spectroscopy

Danielle L. Smiley, Linda J. M. Davis, and Gillian R. Goward\*

Department of Chemistry & Chemical Biology, McMaster University, 1280 Main St. West, Hamilton, Ontario L8S 4M1, Canada

**ABSTRACT:** <sup>6</sup>Li selective inversion NMR experiments are used to reveal Li ion exchange rates and energy barriers for Li ion hopping in monoclinic Li<sub>3</sub>Fe<sub>2</sub>(PO<sub>4</sub>)<sub>3</sub>. The three crystallographically unique Li sites in this material are well resolved by magic-angle spinning, thus allowing for the examination of all three exchange processes. We have revisited this material using selective inversion to probe dynamics, and energy barriers over the temperature range 268–397 K are found to be 0.37 ± 0.07, 0.53 ± 0.02, and 0.52 ± 0.03 eV for the three unique exchange pairs. The results presented here are consistent with the known Li<sub>3</sub>Fe<sub>2</sub>(PO<sub>4</sub>)<sub>3</sub> crystal structure. The selective inversion experiment is more robust than 2D EXSY for the determination of energy barriers by NMR; this can be attributed to the efficiency of the one-dimensional technique, and an exchange model that accounts for multisite exchange and fast spin–lattice relaxation. Moreover, bond valence sum density maps provide a meaningful depiction of lithium ion diffusion pathways in this material that complement the NMR results.



## 1. INTRODUCTION

The rapid development of technology in recent years has necessitated the exploration of new battery technologies in order to keep up with the growing demand for a sustainable energy storage alternative. The popularity of lithium ion batteries for use in electric vehicles and other energy storage applications can be attributed to their high gravimetric and volumetric energy densities as compared to other rechargeable battery alternatives.<sup>1</sup> Of particular interest is the positive electrode (cathode), which, if not chosen carefully, can significantly limit electrochemical performance. Much of the research in the area of cathode materials for Li ion batteries has focused on the development of layered oxide structures such as LiCoO<sub>2</sub><sup>2</sup> and Li[Ni<sub>1/3</sub>Mn<sub>1/3</sub>Co<sub>1/3</sub>]O<sub>2</sub><sup>3</sup> as well as the popular spinel LiMn<sub>2</sub>O<sub>4</sub><sup>4,5</sup> which display impressive voltages and theoretical capacities. It has been demonstrated, however, that a lack of thermal and electrochemical stability in layered oxides<sup>6,7</sup> and capacity fading in the spinel materials<sup>8</sup> may limit their success in larger scale commercial applications. There has thus been considerable development of polyanionic Li<sup>+</sup> intercalation materials that boast a more sophisticated 3-dimensional ion transport mechanism.

The proposal of polyanion frameworks has opened the door for a variety of novel structures that preserve their rigid structural foundation upon electrochemical cycling. This is largely due to the inductive effect of the polyanion tetrahedra that pull oxygen electron density away from the transition metal and mobile lithium ion, thus opening the pathway for Li ion diffusion while maintaining a strong structural framework.<sup>9</sup> Iron-based compounds of this type are ideal due to their low cost and low toxicity relative to other transition metals such as cobalt. In particular, the success of LiFePO<sub>4</sub><sup>10–13</sup> has motivated the investigation of similar polyanion phosphate structures such as LiFePO<sub>4</sub>F,<sup>14</sup> LiFeP<sub>2</sub>O<sub>7</sub>,<sup>15,16</sup> and Li<sub>3</sub>Fe<sub>2</sub>(PO<sub>4</sub>)<sub>3</sub>,<sup>9,17,18</sup> which

take advantage of the Fe<sup>2+</sup>/Fe<sup>3+</sup> redox couple occurring at 3.0, 2.9, and 2.8 V for the three materials, respectively. The monoclinic phase of Li<sub>3</sub>Fe<sub>2</sub>(PO<sub>4</sub>)<sub>3</sub>, which crystallizes with *P*2<sub>1</sub>/*n* symmetry, consists of corner-sharing PO<sub>4</sub> tetrahedra and FeO<sub>6</sub> octahedra, where the lithium ions occupy two distinct 5-coordinate sites and a single 4-coordinate site. Despite initial difficulty achieving the theoretical capacity of 128 mA h<sup>−1</sup> in this material, this obstacle has been largely overcome by efforts to control particle size<sup>19,20</sup> and coat the surface of the active material with conductive carbon.<sup>19</sup> The electrochemical and structural properties of this material have been extensively studied as a function of a variety of parameters.<sup>21–24</sup> The use of computational methods have also aided in the understanding of lithium environments and dynamics as a function of cycling in the monoclinic phase.<sup>25–29</sup> The promising electrochemical and structural properties of this material have motivated the study of Li ion mobility within this material at the molecular level.

Solid-state NMR (ssNMR) is an ideal tool for studying this class of materials, as it is sensitive to the mobile lithium ion as well as the surrounding structural framework. Ion dynamics have been assessed by <sup>6,7</sup>Li ssNMR with two-dimensional exchange spectroscopy (2D EXSY) in Li intercalation materials such as Li<sub>3</sub>Fe<sub>2</sub>(PO<sub>4</sub>)<sub>3</sub>,<sup>30</sup> Li<sub>3</sub>V<sub>2</sub>(PO<sub>4</sub>)<sub>3</sub>,<sup>31</sup> and LiMn<sub>2</sub>O<sub>4</sub><sup>32</sup> to quantify both time scales and energy barriers of Li-ion hopping between crystallographic sites. These energy barriers were correlated to structural properties such as Li–Li internuclear distances, the sharing geometry between Li environments, and the constraints created by any bottlenecks found along the exchange pathway<sup>30,31,33</sup> in order to better understand the structural features that enhance or inhibit ion mobility and

Received: July 28, 2013

Revised: October 14, 2013

Published: October 22, 2013

subsequent electrochemical performance. More recently, the NMR tools used to quantify time scales in these highly paramagnetic materials have expanded to include  ${}^6\text{Li}$  1D EXSY and shaped-pulse selective inversion (SI) methods.<sup>34,35,33</sup> This was largely motivated by a need to bypass the experimental limitations introduced by the inherently short spin–lattice relaxation times of these paramagnetic materials. Although both  ${}^6\text{Li}$  and  ${}^7\text{Li}$  are quadrupolar nuclei, the spin–lattice relaxation is dominated by the dipolar and hyperfine couplings with the paramagnetic metal center,<sup>36</sup> which bring  $T_1$  relaxation times to the micro- or millisecond time scale. This time scale is on par with the rates of ion motion, meaning that extending the mixing times of the 2D EXSY experiments to gain a complete and accurate picture of ion exchange is complicated by the rapidly relaxing Li magnetization. In the 1D SI experiment, the independently measured  $T_1$  rates are included in the fit of the exchange matrix, thereby taking into account the behavior of the magnetization at mixing times longer than the spin–lattice relaxation.

The work presented here describes a series of selective inversion recovery experiments probing ionic motion in the monoclinic phase of  $\text{Li}_3\text{Fe}_2(\text{PO}_4)_3$ , where measured rate constants are used in the calculation of energy barriers for Li ion hopping. The obtained exchange rates are then correlated to Li–Li distances and Li–O bottlenecks. Additionally, the simplified structural picture of the crystal lattice, based on geometric windows for lithium ion hopping and internuclear distances, was shown to be insufficient to justify the similarities/differences in the  $\text{Li}^+$  transport. For this reason, the correlation of NMR results to structural features has expanded to incorporate the role of the charge distribution in the host framework as described by the bond valence density<sup>37–39</sup> both at the Li sites and along the diffusion pathway. These results are compared to our previous study of Li-ion hopping in  $\text{Li}_3\text{Fe}_2(\text{PO}_4)_3$  that used  ${}^6\text{Li}$  2D EXSY to quantify the time scales and energy barriers of ion hopping.

As was revealed by Kim et al.,<sup>26</sup> our original 2D EXSY study had incorrectly assigned the NMR signals, caused by a mislabeling of the crystallographic sites. This has been corrected for the present study. However, this error in the assignment may have masked some of the limitations of  ${}^6\text{Li}$  2D EXSY when applied to strongly paramagnetic systems such as  $\text{Li}_3\text{Fe}_2(\text{PO}_4)_3$ . In particular, we note that the largest activation energy as measured by 2D EXSY was later revealed (in the corrected assignment) to belong to one of the more open diffusion pathways. This counterintuitive result highlighted the possibility that treatment of the 2D data was not accounting for multisite hops, thus inflating the observed energy barrier. The Li ion dynamics in  $\text{Li}_3\text{Fe}_2(\text{PO}_4)_3$  are therefore revisited here using  ${}^6\text{Li}$  one-dimensional selective inversion methods which are found to produce more accurate results that reflect single-site hopping mechanisms through a more rigorous data analysis process.

**1.1. Selective Inversion Recovery Experiments.** While commonly utilized in solution-state NMR,<sup>40,41</sup> the use of selective inversion NMR to study solid-state materials has been largely unexploited. The selective inversion experiment operates by initially inverting a single Li resonance using a soft  $180^\circ$  Gaussian-shaped pulse.<sup>42</sup> The magnetization is then allowed to return to equilibrium over a series of mixing times ( $\tau_{\text{mix}}$ ) during which relaxation can be achieved by a combination of chemical exchange with noninverted Li resonances in addition to spin–lattice relaxation ( $T_1$ ). By

monitoring the magnetization of each site as a function of mixing time, rate constants for ion hopping can be obtained.<sup>43,44</sup> In the case where chemical exchange is occurring, the selectively inverted resonance will demonstrate a buildup of magnetization due to exchange with noninverted exchange partners as well as inherent  $T_1$  relaxation. The noninverted sites, however, will experience an attenuation of intensity due to exchange with the inverted resonance before returning to equilibrium. The superior nature of this technique arises from the fact that the collection of many data points is done in an efficient manner relative to the 2D experiment, allowing us to effectively model relaxation of the magnetization back to equilibrium under a variety of conditions. With 1D SI we rely on accurately fitting the well-defined transient wells developed by the noninverted spins, which is fitted together with an independently measured  $T_1$  relaxation value, to give the overall exchange model, making this a more robust method for quantifying ion dynamics in highly paramagnetic cathode materials for lithium ion batteries.

The work presented here demonstrates the effectiveness of the selective inversion recovery experiment for the investigation of exchange rates in Li cathode materials in an efficient manner relative to traditional two-dimensional techniques with monoclinic  $\text{Li}_3\text{Fe}_2(\text{PO}_4)_3$ . It is important to note that, ultimately, ion transport governs the efficiency of any electrochemical device, and thus, a site specific method of quantification is an important tool for evaluating these structures.

**1.2. Bond Valence Sums.** The concept of bond valence sum as first described by Brown and Shannon in the 1970s is a useful way of visualizing bonding strength in a variety of inorganic crystal structures. The empirical relationship between an atom's bond valence and the associated bond length allow for the determination of relative bond valences.<sup>37,38</sup> For a given atom in a crystalline lattice, a bond valence sum as determined by known bond lengths could be thought of as a measure of how tightly bound said ion is within its crystallographic site.<sup>45</sup> Gonzales-Platas et al.<sup>39</sup> have developed the program VALMAP to calculate the theoretical bond valence sum of a given atom if it were to sit at any point within the lattice allowing a bond valence sum map to be generated in order to visualize favorable positions for the atom of interest. The bond valence sum calculation for an ion at any position within a lattice can be determined by the following equation

$$V_i = \sum_j \exp\left(\frac{R_0 - R_j}{b}\right)$$

where  $R_0$  and  $R_j$  are the nominal and observed bond lengths, respectively, and  $b$  is effectively a measure of the softness of the atom interactions.

Bond valence sums are particularly relevant when applied to solid-state lithium ion battery materials, as the valence of the mobile lithium ion may affect its ability to move freely throughout the crystal lattice and thus be useful for energy applications. It is expected that a lithium ion with a calculated bond valence sum that is greater than +1.00 should be more tightly held within its crystallographic position than a Li ion with a bond valence sum value of less than 1.00, indicating weaker average bonding interactions. Furthermore, by mapping out potential bond valence sum values along exchange pathways in multisite materials, favorable lithium ion exchange pairs can be identified. The present work demonstrates that it is

possible to correlate experimentally determined energy barriers for lithium ion hopping with bond valence sum pathways as mapped out using VALMAP.

The use of a bond valence sum models to understand lithium ion diffusion pathways in cathodes allows for a visualization of the Coulombic interactions, based on the crystal structure itself. Other groups have successfully utilized computational methods based on atomistic simulation techniques,<sup>46</sup> for evaluating dynamics in Li ion cathode materials. In such calculations, the energy of the Li ion migration along a selected diffusion path is calculated and activation energies predicted based on the highest potential energy point along the preferred path. The bond valence sum method is used here to support the interpretation of the experimental activation energy results obtained by NMR, where the structural Li–O contacts are used to predict how strongly held a Li atom is within its crystallographic position.

## 2. EXPERIMENTAL SECTION

**2.1. Sample Preparation.**  $\text{Li}_3\text{Fe}_2(\text{PO}_4)_3$  was prepared by the previously reported high-temperature solid-state synthesis as described by Padhi et al.<sup>9</sup> Stoichiometric amounts of LiOH monohydrate,  $\text{Fe}_2\text{O}_3$ , and  $\text{NH}_4\text{H}_2\text{PO}_4$  were ground together and heated to 250 °C for 4 h to drive off water and ammonia. The sample was reground and heated to 850 °C for 2 days, following which a third heating step at 930 °C for 24 h was carried out.

**2.2. Solid-State NMR.** All variable-temperature  $^6\text{Li}$  MAS NMR spectra were acquired at a Larmor frequency of 44.1 MHz on a Bruker AV-300 spectrometer using a custom-built double-resonance probe supporting rotors 1.8 mm in diameter. Temperatures were calibrated using  $\text{Sm}_2\text{Sn}_2\text{O}_7$  according to the method discussed previously by Gray et al.<sup>47</sup> One-dimensional  $^6\text{Li}$  MAS spectra were obtained using a Hahn-echo pulse sequence with a 90° pulse of 3  $\mu\text{s}$  and a recycle delay of 200 ms.  $^6\text{Li}$  selective inversion recovery spectra were acquired using the 180°– $\tau_{\text{mix}}$ –90° sequence, where the 180° Gaussian shaped pulse was 1 ms in length with a soft pulse power of 0.109 W. The mixing time was varied across a series of experiments and was chosen to range from 5  $\mu\text{s}$  to 200 ms. A hard, 3  $\mu\text{s}$  90° pulse was used to acquire the final signal.

**2.3. Data Analysis using CIFIT.** Data collected from selective inversion recovery experiments were modeled using the CIFIT program developed by A. D. Bain at McMaster University. CIFIT uses the observed intensities for all sites in the NMR spectrum as a function of mixing time and determines the lithium ion jump rates ( $k$ ), the spin–lattice relaxation times ( $T_1$ ) in the absence of chemical exchange, as well as the difference in magnetization between initial ( $M_i(0)$ ) and equilibrium ( $M_i(\infty)$ ) conditions. CIFIT utilizes a rate matrix that describes the relaxation of spins under the influence of chemical exchange. The relevant parameters are varied using the Levenberg–Marquardt algorithm in this model and compared with experimental data in order to minimize the sum of the square of the difference.

## 3. RESULTS AND DISCUSSION

The one-dimensional  $^6\text{Li}$  MAS spectrum of  $\text{Li}_3\text{Fe}_2(\text{PO}_4)_3$  shown in Figure 1 consists of three resonances, labeled A, B, and C, with paramagnetic shifts of 41, 94, and 203 ppm, respectively. Assignment of these resonances to their crystallographic sites is based on the hyperfine coupling between the Li

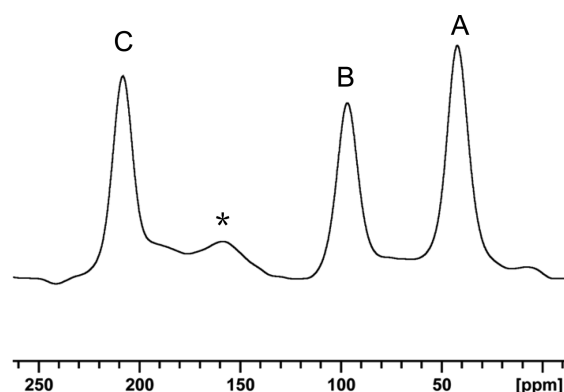


**Figure 1.**  $^6\text{Li}$  MAS (20 kHz) spectrum of  $\text{Li}_3\text{Fe}_2(\text{PO}_4)_3$  at 289 K indicating the three well-resolved Li resonances corresponding to the three unique crystallographic Li sites in the structure.

ions and the paramagnetic center and has been corrected from our original work<sup>30</sup> in light of the results presented by Kim et al.<sup>26</sup> More generally, the subtleties of determining accurate chemical shift assignments in polyanionic structures, such as the one presented here, have been the focus of recent density functional theory calculations by Middlemiss and coauthors.<sup>48</sup> From this point forward, when referring to both the present 1D SI results as well as the original 2D EXSY study, we will use the correctly labeled and simplified notation throughout the discussion where the crystallographic site is stated with its corresponding Li NMR signal shown as a subscript letter ( $\text{Li}_{3\text{A}}$ ,  $\text{Li}_{2\text{B}}$ , and  $\text{Li}_{1\text{C}}$ ) as outlined in Table 1.

**Table 1. Assignment of Li Signals to Crystallographic Sites within the  $\text{Li}_3\text{Fe}_2(\text{PO}_4)_3$  Framework<sup>a</sup>**

resonance signal	paramagnetic shift (ppm)	old (incorrect) assignment <sup>30</sup>	new assignment <sup>26</sup>
A	41	Li3	$\text{Li}_{3\text{A}}$
B	94	Li1	$\text{Li}_{2\text{B}}$
C	203	Li2	$\text{Li}_{1\text{C}}$

<sup>a</sup>Also included is the original, incorrect assignment, from the previously published 2D EXSY work.<sup>30</sup>

Previous 2D EXSY experiments revealed exchange between all three crystallographic Li sites corresponding to  $\text{Li}_{3\text{A}}$ – $\text{Li}_{2\text{B}}$ ,  $\text{Li}_{3\text{A}}$ – $\text{Li}_{1\text{C}}$ , and  $\text{Li}_{2\text{B}}$ – $\text{Li}_{1\text{C}}$  exchange pairs. This evidence of the lithium ions undergoing an appreciable amount of exchange even at low temperatures coupled with well-resolved Li signals make selective inversion experiments a feasible alternative for studying chemical exchange in this system. A comparison of the nonselective inversion (NSI) buildup curves for a single Li resonance to the selective inversion (SI) analogue in Figure 2 clearly indicates a difference in relaxation rate of the magnetization as a function of temperature in the selective inversion case that is not observed for the nonselective inversion data set. This is explained by a difference in experimental conditions, where in the NSI experiment the return of the magnetization to equilibrium is primarily governed by the inherent  $T_1$  behavior of each site, which does not change with temperature. Conversely, the buildup of magnetization changes as a function of temperature when a site is selectively inverted as relaxation in the SI experiment is affected by chemical exchange with noninverted spins, which is expected to be temperature dependent.



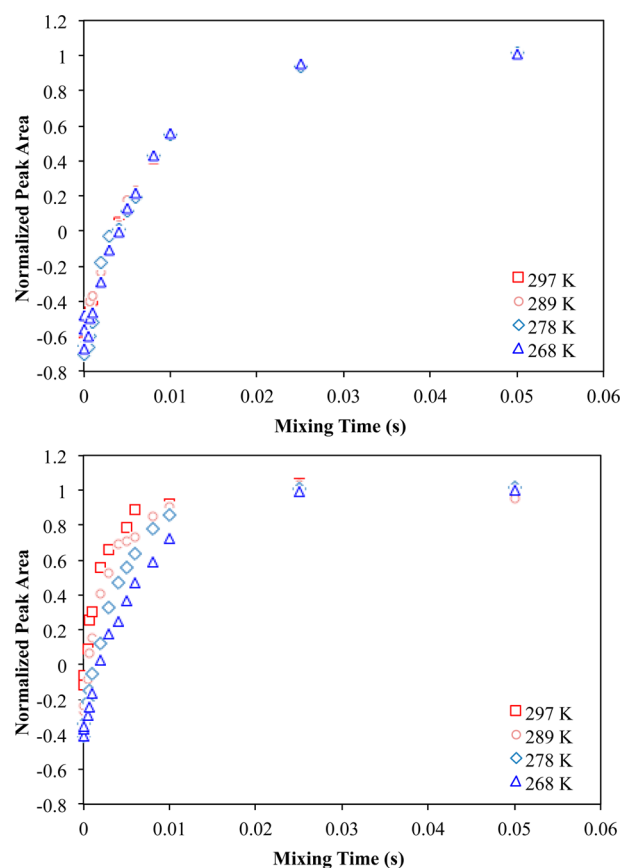


**Figure 2.** Buildup curves of peak C intensity over four temperatures comparing a nonselective inversion experiment (top) to a selective inversion experiment (bottom).

A complete set of selective inversion experiments were carried out across a range of temperatures where in each case all three sites were selectively inverted and their subsequent return to equilibrium was monitored. The magnetization of the noninverted sites was then plotted for each temperature as a function of mixing time, where a characteristic transient decrease in intensity is observed in all cases. Upon inversion of a single site, for example site C, the transient magnetization at sites A and B are plotted and modeled to yield AC and BC rate constants. Figure 3 depicts the experimental and modeled curves for AB, AC, and BC exchange upon inversion of sites A (for AB exchange) and C (for AC and BC exchange). Importantly, the depth of the transient well, or the degree of attenuation, increases as exchange with the inverted site becomes more rapid at higher temperatures. It should be noted that at low temperatures a slow exchange rate causes only a small change in magnetization at the noninverted sites that is difficult to observe before spin–lattice relaxation processes take over. There are thus unreasonably high errors associated with modeling the data from temperatures lower than those used herein. Significant scattering at low temperatures, particularly for the AB exchange pair, is attributed to the 60 ppm separation between these sites (compared to 120 and 175 ppm, respectively, for the BC and AC pairs at 268 K), thus making small differences in intensity at neighboring sites difficult to identify. Conversely, at temperatures higher than 298 K, the rate of exchange is relatively fast, causing unreliable results due to coalescence of the peaks, again making it difficult to selectively invert a single site. The temperature range used was

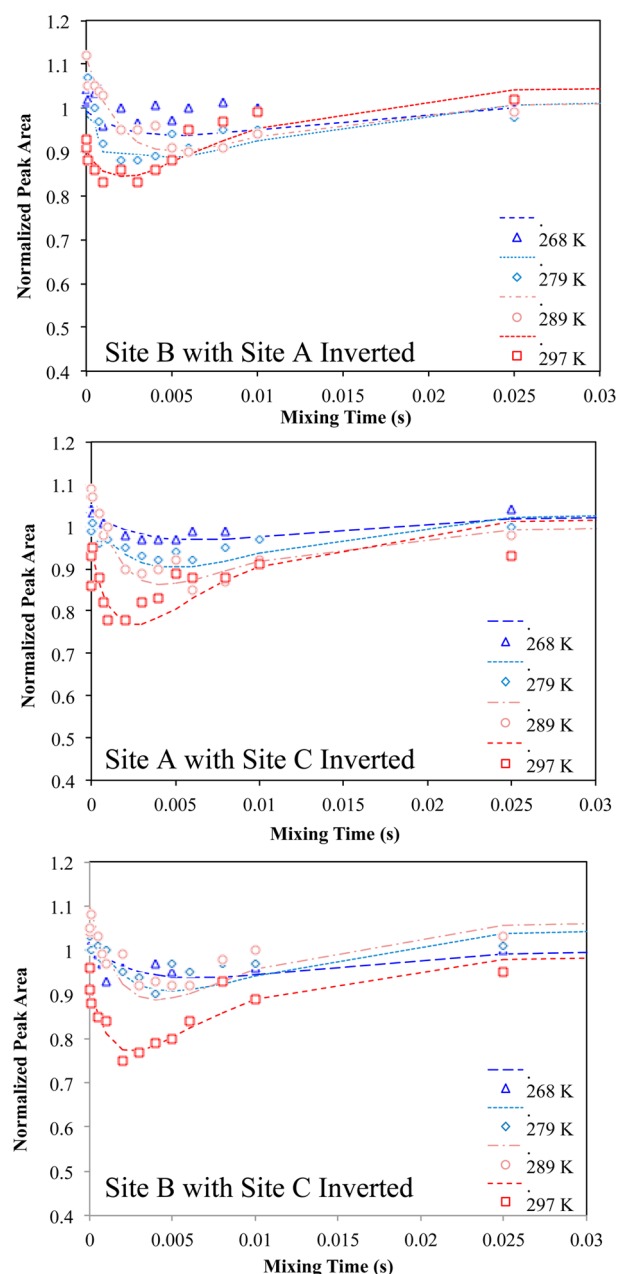


**Figure 3.** Transient curves resulting from the change in magnetization at the noninverted sites during a selective inversion experiment at various temperatures. From top to bottom the graphs correspond to magnetization at site B upon inversion of A (top), magnetization at A upon inversion of C (middle), and magnetization at B upon inversion of C (bottom) yielding rate constants for the AB, AC, and BC pairs, respectively, at 268, 279, 289, and 297 K. The points in each graph represent experimentally obtained peak areas, while the lines represent the model done in CIFIT.

therefore chosen based on the limitations on accurate data collection due to negligible exchange at the low end and beginning coalescence of peaks at the upper temperature limit. Rate constants for the  $\text{Li3}_\text{A}$ – $\text{Li1}_\text{B}$ ,  $\text{Li3}_\text{A}$ – $\text{Li1}_\text{C}$ , and  $\text{Li2}_\text{B}$ – $\text{Li1}_\text{C}$  exchange processes are measured by modeling the experimental data with CIFIT, which indicated exchange was on the order of  $20 \text{ s}^{-1}$  at 268 K and as fast as  $200 \text{ s}^{-1}$  at room temperature. An Eyring analysis was used to treat the data, where by fitting the experimentally measured rate constants as a function of temperature, activation energies for the hopping of Li ions

between the three crystallographic positions are determined as shown by the Eyring plots in Figure 4. The results of the present selective inversion NMR study (Table 2) indicate low energy barriers for all exchange pairs,  $\text{Li3}_\text{A}$ – $\text{Li2}_\text{B}$  being the lowest energy and  $\text{Li3}_\text{A}$ – $\text{Li1}_\text{C}$  and  $\text{Li2}_\text{B}$ – $\text{Li1}_\text{C}$  being higher than  $\text{Li3}_\text{A}$ – $\text{Li2}_\text{B}$ , and equal to each other within error.

The significantly lower activation energy for  $\text{Li3}_\text{A}$ – $\text{Li2}_\text{B}$  exchange as compared to the  $\text{Li3}_\text{A}$ – $\text{Li1}_\text{C}$  or  $\text{Li2}_\text{B}$ – $\text{Li1}_\text{C}$  pairs

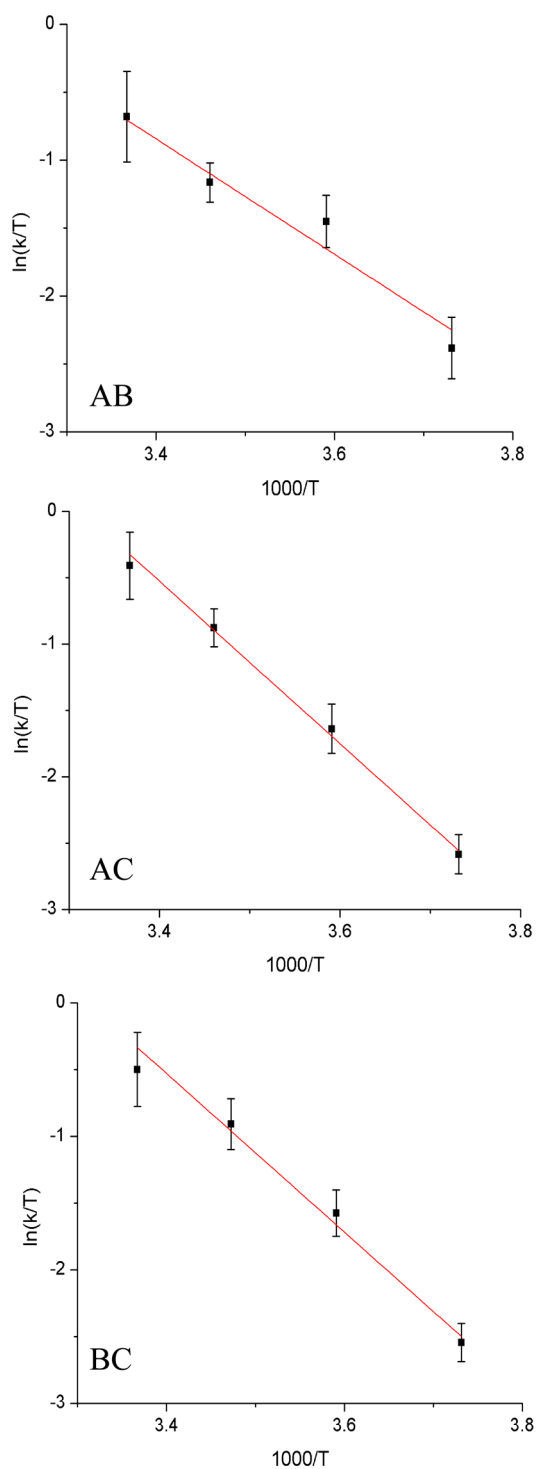


**Figure 4.** Eyring plots and corresponding linear fits for the  $\text{Li3}_\text{A}$ – $\text{Li2}_\text{B}$  (top),  $\text{Li3}_\text{A}$ – $\text{Li1}_\text{C}$  (middle), and  $\text{Li2}_\text{B}$ – $\text{Li1}_\text{C}$  (bottom) exchange pairs in  $\text{Li}_3\text{Fe}_2(\text{PO}_4)_3$  as determined by selective inversion.

**Table 2.** Summary of Activation Energies in  $\text{Li}_3\text{Fe}_2(\text{PO}_4)_3$  for  $\text{Li3}_\text{A}$ – $\text{Li2}_\text{B}$ ,  $\text{Li3}_\text{A}$ – $\text{Li1}_\text{C}$ , and  $\text{Li2}_\text{B}$ – $\text{Li1}_\text{C}$  Hopping As Determined by Selective Inversion (SI)

exchange pair	$E_a$ (eV)	$k_{268\text{ K}}$ ( $\text{s}^{-1}$ )	$k_{297\text{ K}}$ ( $\text{s}^{-1}$ )
$\text{Li3}_\text{A}$ – $\text{Li2}_\text{B}$	$0.37 \pm 0.07$	$25 \pm 5$	$150 \pm 50$
$\text{Li3}_\text{A}$ – $\text{Li1}_\text{C}$	$0.53 \pm 0.02$	$20 \pm 3$	$200 \pm 50$
$\text{Li2}_\text{B}$ – $\text{Li1}_\text{C}$	$0.52 \pm 0.03$	$20 \pm 3$	$180 \pm 50$

can be aptly explained by the known structural features of the local lithium environments. The low-energy  $\text{Li3}_\text{A}$ – $\text{Li2}_\text{B}$  exchange pair corresponds to the shortest Li–Li internuclear distance, consistent with the lower energy barrier for exchange of these two ions as it is expected that a shorter distance requires less energy for ion hopping. In addition, a lithium–oxygen (Li–O) bottleneck area can be calculated, which is simply the area of the face that the mobile lithium ions share when exchanging with their respective partners. A relatively small Li–O bottleneck should correspond to a higher energy exchange process due to the repulsive effect of neighboring oxygen atoms, thereby making exchange energetically costly. This turns out to be the case, where the most open Li–O bottleneck ( $4.22 \text{ \AA}^2$ ) corresponds to the lowest energy exchange process ( $\text{Li3}_\text{A}$ – $\text{Li2}_\text{B}$ ).

Table 3 summarizes the relevant Li–Li distances, Li–O bottleneck sizes, and their respective activation energies. While

**Table 3.** Summary of Structural Parameters for Li Sites within the Monoclinic  $\text{Li}_3\text{Fe}_2(\text{PO}_4)_3$  Structure

lithium pair	energy barrier (eV)	Li–Li distance ( $\text{\AA}$ )	Li–O bottleneck ( $\text{\AA}^2$ )	BVS values
$\text{Li2}_\text{B}$ – $\text{Li3}_\text{A}$	$0.37 \pm 0.07$	3.11	4.22	0.952 ( $\text{Li2}_\text{B}$ ) 0.989 ( $\text{Li3}_\text{A}$ )
$\text{Li1}_\text{C}$ – $\text{Li3}_\text{A}$	$0.53 \pm 0.02$	3.42	3.61	1.054 ( $\text{Li1}_\text{C}$ ) 0.989 ( $\text{Li3}_\text{A}$ )
$\text{Li1}_\text{C}$ – $\text{Li2}_\text{B}$	$0.52 \pm 0.032$	3.14	3.96	1.054 ( $\text{Li1}_\text{C}$ ) 0.952 ( $\text{Li2}_\text{B}$ )

the trend in energy barriers is consistent with the observed structural constraints, the  $\text{Li3}_\text{A}$ – $\text{Li2}_\text{B}$  and  $\text{Li2}_\text{B}$ – $\text{Li1}_\text{C}$  pairs have very similar Li–Li distances and Li–O bottlenecks. It therefore is unlikely that these parameters alone can explain the significantly higher activation energy for the  $\text{Li2}_\text{B}$ – $\text{Li1}_\text{C}$  pair when the crystallographic information is similar for both exchange pairs. A third structural parameter, bond valence sum (BVS) values, can therefore be considered, in an effort to account for the difference in energy barriers.

For a typical lithium ion, BVS values center around +1.000, where values larger than this indicate a lithium ion that is more tightly bound, and smaller values indicate an ion which might move more readily from its crystallographic position. BVS values were calculated for all three lithium sites in this structure with an  $R_0$  of  $1.466 \text{ \AA}$  and  $b = 0.37$ . The calculated bond valence sums are outlined in Table 3 and are found to correlate well to the observed energy barriers for Li ion hopping. The  $\text{Li1}_\text{C}$  ion has the highest BVS value of 1.054, and all exchange processes involving this site require significantly more energy, consistent with this ion being tightly held within its crystallographic site. The  $\text{Li2}_\text{B}$ – $\text{Li3}_\text{A}$  exchange pair requires the smallest amount of energy, and both sites involved in this process have low BVS values (0.952 and 0.989, respectively), indicating their ability to travel readily through the structure. The activation energies determined here by NMR are

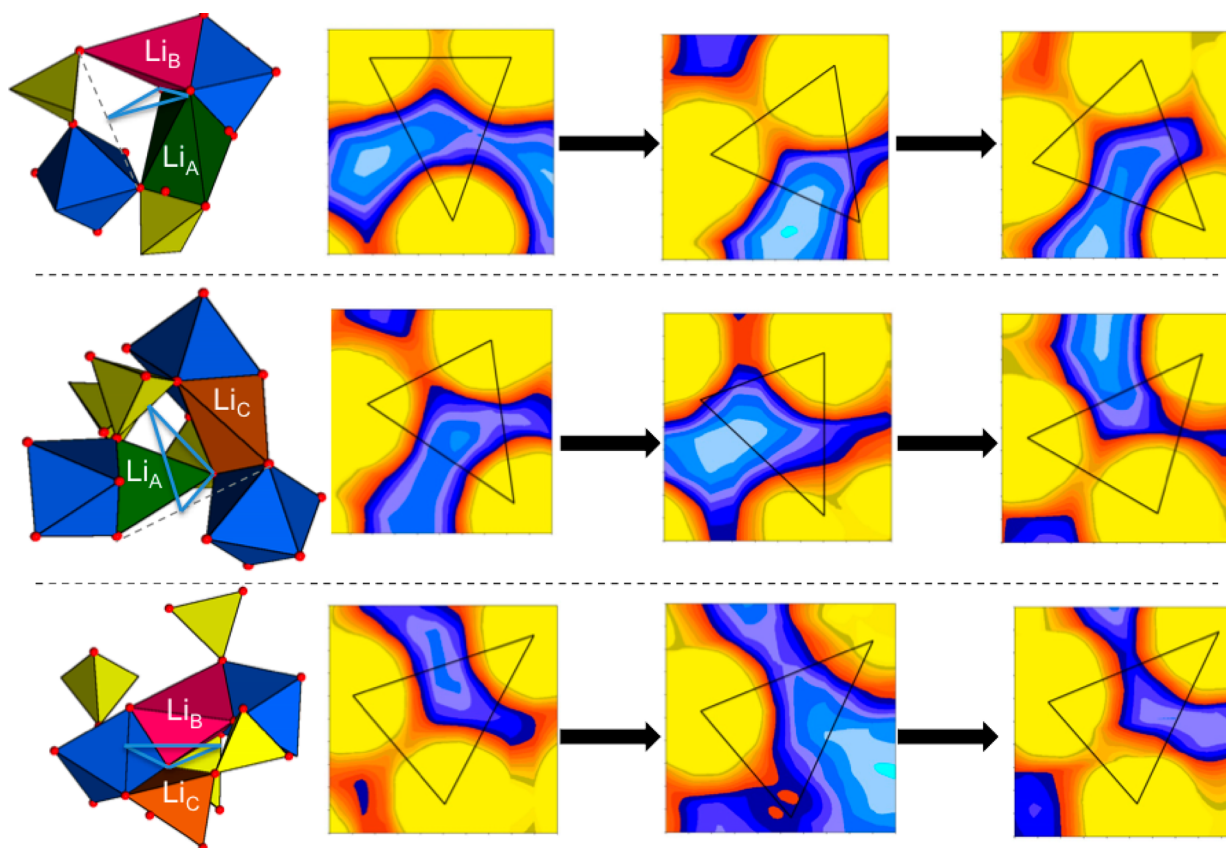


**Figure 5.** Bond valence sum (BVS) maps depicting the pathway for Li ion hopping in terms of bond valence sum density. The yellow-orange regions correspond to areas of high bond valence sum density, while the blue-light blue corresponds to areas of low bond valence sum density. The consecutive images shown above demonstrate the bond valence sum at the start, midpoint, and end of each given ion pair exchange path. Lithium ions that encounter regions of relatively low bond valence sum density will exchange more favorably.

consistent with these BVS values, with the most tightly held ion as determined by the bond valence method requiring the most energy to hop between sites. Results are comparable to the computational work of Islam and coauthors,<sup>46</sup> where the Li ion exchange activation energies are found to be within the typical range for an Fe phosphate cathode material.

While the use of a simple BVS value for each crystallographic Li position provides a quantitative interpretation for the observed energy barriers as determined here by NMR, qualitative maps can be generated, which provide an intuitive visualization of the BVS density along the Li ion exchange pathways. As such, a sequence of BVS density maps have been generated using VALMAP to visualize the BVS density along the expected Li exchange pathway for each exchange pair. Figure 5 maps out BVS density along the expected pathway for Li ion diffusion by depicting the face that each Li exchange partner is seeing at different points along the trajectory of the mobile ion. Based on the BVS density mapping along the relevant Li ion channels, all three exchange pathways are relatively open for exchange, consistent with the low activation energies and moderately fast exchange observed even at low temperatures. In particular, the BVS density maps can be used to justify the difference in activation energy between pairs within this structure. The similar Li–Li distances and two-dimensional Li–O bottleneck sizes of the  $\text{Li3}_\text{A}$ – $\text{Li2}_\text{B}$  and  $\text{Li2}_\text{B}$ – $\text{Li1}_\text{C}$  pairs (described above) do not adequately explain the substantial increase in energy barrier for the  $\text{Li2}_\text{B}$ – $\text{Li1}_\text{C}$  pair. According to the BVS density maps for the ion pathways, the  $\text{Li2}_\text{B}$ – $\text{Li1}_\text{C}$  pair has higher BVS density along the entirety of the

exchange pathway as compared to the  $\text{Li3}_\text{A}$ – $\text{Li2}_\text{B}$  pair, indicating diffusion along this pathway is somewhat limited. This improves the consistency of the structural and transport models. Previously, the high  $\text{Li3}_\text{A}$ – $\text{Li2}_\text{B}$  energy barrier of  $0.81 \pm 0.04$  eV measured by 2D EXSY was more than double the result for the same exchange pair found by the 1D SI method (Table 4), suggesting a multisite exchange model is necessary

**Table 4. Comparison of Energy Barriers Determined from 1D SI Measurements of the Present Work and the Previously Published 2D EXSY Results**

$E_a$ (eV)		
2D EXSY results <sup>30</sup>	1D SI results	correct assignment <sup>26</sup>
$0.81 \pm 0.04$	$0.37 \pm 0.07$	$\text{Li3}_\text{A}$ – $\text{Li2}_\text{B}$
$0.63 \pm 0.03$	$0.53 \pm 0.02$	$\text{Li3}_\text{A}$ – $\text{Li1}_\text{C}$
$0.59 \pm 0.05$	$0.52 \pm 0.03$	$\text{Li2}_\text{B}$ – $\text{Li1}_\text{C}$

to accurately describe ion diffusion in this material. Here, we have shown that the single-site exchange between  $\text{Li3}_\text{A}$ – $\text{Li2}_\text{B}$  in fact has the lowest energy barrier, consistent with its low BVS pathway. A three-dimensional ion transport mechanism is supported both by the activation energies and by BVS density maps, where an ion diffusion pathway between the three Li sites can be envisioned. This 3D ion transport mechanism is expected to be advantageous upon implementation in commercial battery technologies, as site defects will not impede overall Li ion diffusion through the cathode structure.



#### 4. CONCLUSIONS

The present study demonstrates the effectiveness of the selective inversion recovery technique for the study of chemical exchange in paramagnetic cathode material monoclinic  $\text{Li}_3\text{Fe}_2(\text{PO}_4)_3$ . The lithium ion hopping rates are found to fall between 20 and 200  $\text{s}^{-1}$  over the temperature range of 265–298 K, with the energy barriers for ion hopping being  $0.37 \pm 0.07$ ,  $0.53 \pm 0.02$ , and  $0.52 \pm 0.03$  eV for the  $\text{Li}_{3\text{A}}\text{--Li}_{2\text{B}}$ ,  $\text{Li}_{3\text{A}}\text{--Li}_{1\text{C}}$ , and  $\text{Li}_{2\text{B}}\text{--Li}_{1\text{C}}$  pairs, respectively. It is clear that the 1D SI results are more accurate, as they are consistent Li–Li internuclear distances, Li–O bottlenecks, and calculated bond valence sum values for each site. Furthermore, it is demonstrated that bond valence sum maps can be utilized in order to gain a complete picture of ion diffusion pathways, which correlate well with the activation energies measured by NMR. This work emphasizes the advantage of using an efficient one-dimensional technique as well as an exchange model that accounts for all relevant relaxation processes, including multisite exchange and spin–lattice relaxation. This is especially critical when probing fast ion mobility in a quickly relaxing system. Evaluating local ion dynamics is key to understanding macroscopic device efficiencies, making selective inversion  $^6,7\text{Li}$  NMR a valuable tool for ion transport assessment in lithium ion cathode materials.

#### AUTHOR INFORMATION

##### Corresponding Author

\*E-mail: goward@mcmaster.ca. Phone: (905)-525-9140 x 24176. Fax: (905)-522-2509.

##### Notes

The authors declare no competing financial interest.

#### ACKNOWLEDGMENTS

The authors are grateful to A. D. Bain for numerous helpful discussions, and for reviewing the manuscript. G.R.G. acknowledges support through the NSERC DG program.

#### REFERENCES

- (1) Tarascon, J.-M.; Armand, M. Issues and Challenges Facing Rechargeable Lithium Batteries. *Nature* **2001**, *414*, 359–367.
- (2) Ohzuku, T.; Ueda, A.; Nagayama, M.; Iwakoshi, Y.; Komori, H. Comparative Study of  $\text{LiCoO}_2$ ,  $\text{LiNi}_{1/2}\text{Co}_{1/2}\text{O}_2$  and  $\text{LiNiO}_2$  for 4 V Secondary Lithium Cells. *Electrochim. Acta* **1993**, *9*, 1159–1167.
- (3) Ohzuku, T.; Makimura, Y. Layered Lithium Insertion Material of  $\text{LiCo}_{1/3}\text{Ni}_{1/3}\text{Mn}_{1/3}\text{O}_2$  for Lithium-Ion Batteries. *Chem. Lett.* **2001**, 642–643.
- (4) Tarascon, J. M.; Wang, E.; Shokoohi, F. K.; McKinnon, W. R.; Colson, S. The Spinel Phase of  $\text{LiMn}_2\text{O}_4$  as a Cathode in Secondary Lithium Cells. *J. Electrochem. Soc.* **1991**, *138*, 2859–2864.
- (5) Thackeray, M. M. Structural Considerations of Layered and Spinel Lithiated Oxides for Lithium Ion Batteries. *J. Electrochem. Soc.* **1995**, *142*, 2558–2563.
- (6) Dahn, J. R.; Fuller, E. W.; Obrovac, M.; von Sacken, U. Thermal Stability of  $\text{Li}_x\text{CoO}_2$ ,  $\text{Li}_x\text{NiO}_2$  and  $\lambda\text{-MnO}_2$  and Consequences for the Safety of Li-ion Cells. *Solid State Ionics* **1994**, *69*, 265–270.
- (7) Wang, L.; Maxisch, T.; Ceder, G. A First-Principles Approach to Studying the Thermal Stability of Oxide Cathode Materials. *Chem. Mater.* **2007**, *19*, 543–552.
- (8) Xia, Y.; Zhou, Y.; Yoshio, M. Capacity Fading on Cycling of 4V  $\text{Li/LiMn}_2\text{O}_4$  Cells. *J. Electrochem. Soc.* **1997**, *144*, 2593–2600.
- (9) Padhi, A. K.; Nanjundaswamy, K. S.; Masquelier, C.; Okada, S.; Goodenough, J. B. Effect of Structure on the  $\text{Fe}^{3+}/\text{Fe}^{2+}$  Redox Couple in Iron Phosphates. *J. Electrochem. Soc.* **1997**, *144*, 1609–1613.
- (10) Padhi, A. K.; Nanjundaswamy, K. S.; Goodenough, J. B. Phospho-olivines as Positive-Electrode Materials for Rechargeable Lithium Batteries. *J. Electrochem. Soc.* **1997**, *144*, 1188–1194.
- (11) Yamada, A.; Chung, S. C.; Hinokuma, K. Optimized  $\text{LiFePO}_4$  for Lithium Battery Cathodes. *J. Electrochem. Soc.* **2001**, *148*, A224–A229.
- (12) Yang, S.; Zavalij, P. Y.; Whittingham, M. S. Hydrothermal Synthesis of Lithium Iron Phosphate Cathodes. *Electrochem. Commun.* **2001**, *3*, 505–508.
- (13) Kang, B.; Ceder, G. Battery Materials for Ultrafast Charging and Discharging. *Nature* **2009**, *458*, 190–193.
- (14) Ramesh, T. N.; Lee, K. T.; Ellis, B. L.; Nazar, L. F. Tavorite Lithium Iron Fluorophosphate Cathode Materials: Phase Transition and Electrochemistry of  $\text{LiFePO}_4\text{F}\text{--Li}_2\text{FePO}_4\text{F}$ . *Electrochem. Solid-State Lett.* **2010**, *13*, A43–A47.
- (15) Wurm, C.; Morcrette, M.; Rousse, G.; Dupont, L.; Masquelier, C. Lithium Insertion/Extraction into/from  $\text{LiMX}_2\text{O}_7$  Compositions ( $\text{M}=\text{Fe}$ , V;  $\text{X}=\text{P}$ , As) Prepared via a Solution Method. *Chem. Mater.* **2002**, *14*, 2701–2710.
- (16) Padhi, A. K.; Nanjundaswamy, K. S.; Masquelier, C.; Okada, S.; Goodenough, J. B. Effect of Structure on the  $\text{Fe}^{3+}/\text{Fe}^{2+}$  Redox Couple in Iron Phosphates. *J. Electrochem. Soc.* **1997**, *144*, 1609–1613.
- (17) Nanjundaswamy, K. S.; Padhi, A. K.; Goodenough, J. B.; Okada, S.; Ohtsuka, H.; Arai, H.; Yamaki, J. Synthesis, Redox Potential Evaluation and Electrochemical Characteristics of NASICON-related-3D Framework Compounds. *Solid State Ionics* **1996**, *92*, 1–10.
- (18) Patoux, S.; Wurm, C.; Morcrette, M.; Rousse, G.; Masquelier, C. A Comparative Structural and Electrochemical Study of Monoclinic  $\text{Li}_3\text{Fe}_2(\text{PO}_4)_3$  and  $\text{Li}_3\text{V}_2(\text{PO}_4)_3$ . *J. Power Sources* **2003**, *119–121*, 278–284.
- (19) Morcrette, M.; Wurm, C.; Masquelier, C. On the way to Optimization of  $\text{Li}_3\text{Fe}_2(\text{PO}_4)_3$  Positive Electrode Materials. *Solid State Sci.* **2002**, *4*, 239–246.
- (20) Cabana, J.; Shirakawa, J.; Masanobu, N.; Wakiyara, M.; Grey, C. P. Effect of Ball-milling and Lithium Insertion on the Lithium Mobility and Structure of  $\text{Li}_3\text{Fe}_2(\text{PO}_4)_3$ . *J. Mater. Chem.* **2011**, *21*, 10012–10020.
- (21) Plylahan, N.; Vidal-Abarca, C.; Lavela, P.; Tirado, J. L. Chromium Substitution in Ion Exchanged  $\text{Li}_3\text{Fe}_2(\text{PO}_4)_3$  and the Effects on the Electrochemical Behaviour as Cathodes for Lithium Batteries. *Electrochim. Acta* **2012**, *62*, 124–131.
- (22) Masquelier, C.; Padhi, A. K.; Nanjundaswamy, K. S.; Goodenough, J. B. New Cathode Materials for Rechargeable Lithium Batteries: The 3-D Framework Structures  $\text{Li}_3\text{Fe}_2(\text{XO}_4)_3$  ( $\text{X}=\text{P}$ , As). *J. Solid State Chem.* **1998**, *135*, 228–234.
- (23) Manthiram, A.; Goodenough, J. B. Lithium Insertion into  $\text{Fe}_2(\text{MO}_4)_3$  Frameworks: Comparison of  $\text{M}=\text{W}$  with  $\text{M}=\text{Mo}$ . *J. Solid State Chem.* **1987**, *71*, 349–360.
- (24) Rousse, G.; Rodriguez-Carvajal, J.; Wurm, C.; Masquelier, C. Magnetic, Structural Studies of the Two Polymorphs of  $\text{Li}_3\text{Fe}_2(\text{PO}_4)_3$ : Analysis of the Magnetic Ground State from Super-Super Exchange Interactions. *Chem. Mater.* **2001**, *13*, 4527–4536.
- (25) Shirakawa, J.; Nakayama, M.; Wakiyara, M.; Yoshiharu, U. Changes in Electronic Structure upon Li Insertion Reaction of Monoclinic  $\text{Li}_3\text{Fe}_2(\text{PO}_4)_3$ . *J. Phys. Chem. B* **2006**, *110*, 17743–17750.
- (26) Kim, J.; Middlemiss, D. S.; Chernova, N. A.; Zhu, B. Y. X.; Masquelier, C.; Grey, C. P. Linking Local Environments and the Hyperfine Shifts: A Combined Experimental and Theoretical  $^{31}\text{P}$  and  $^7\text{Li}$  Solid-State NMR Study of Paramagnetic Fe(III) Phosphates. *J. Am. Chem. Soc.* **2010**, *132*, 16825–16840.
- (27) Castets, A.; Carlier, D.; Trad, K.; Delmas, C.; Menetrier, M. Analysis of the  $^7\text{Li}$  NMR signals in the Monoclinic  $\text{Li}_3\text{Fe}_2(\text{PO}_4)_3$  and  $\text{Li}_3\text{V}_2(\text{PO}_4)_3$  Phases. *J. Phys. Chem. C* **2010**, *114*, 19141–19150.
- (28) Morgan, D.; Ceder, G.; Saidi, M. Y.; Barker, J.; Swyer, J.; Huang, H.; Adamson, G. Experimental and Computational Study of the Structure and Electrochemical Properties of Monoclinic  $\text{Li}_3\text{M}_2(\text{PO}_4)_3$  Compounds. *J. Power Sources* **2003**, *119–121*, 755–759.
- (29) Hautier, G.; Jain, A.; Ping Ong, S.; Kang, B.; Moore, C.; Doe, R.; Ceder, G. Phosphates as Lithium-Ion Battery Cathodes: An Evaluation

Based on High-Throughput *ab initio* Calculations. *Chem. Mater.* **2011**, *23*, 3495–3508.

(30) Davis, L. J. M.; Heinmaa, I.; Goward, G. R. Study of Lithium Dynamics in Monoclinic  $\text{Li}_3\text{Fe}_2(\text{PO}_4)_3$  using  $^6\text{Li}$  VT and 2D Exchange MAS NMR Spectroscopy. *Chem. Mater.* **2010**, *22*, 769–775.

(31) Cahill, L. S.; Chapman, R. P.; Britten, J. F.; Goward, G. R.  $^7\text{Li}$  NMR and Two-Dimensional Exchange Study of Lithium Dynamics in Monoclinic  $\text{Li}_3\text{V}_2(\text{PO}_4)_3$ . *J. Phys. Chem. B* **2006**, *110*, 7171–7177.

(32) Verhoeven, V. W. J.; de Schepper, I. M.; Nachtegall, G.; Kentgens, A. P. M.; Kelder, E. M.; Schoonman, J.; Mulder, F. M. Lithium Dynamics in  $\text{LiMn}_2\text{O}_4$  Probed Directly by Two-Dimensional  $^7\text{Li}$  NMR. *Phys. Rev. Lett.* **2001**, *86*, 4314–4317.

(33) Davis, L. J. M.; Goward, G. R. Differentiating Lithium Ion Hopping Rates in Vanadium Phosphate versus Vanadium Fluorophosphate Structures Using 1D  $^6\text{Li}$  Selective Inversion NMR. *J. Phys. Chem. C* **2013**, *117*, 7981–7992.

(34) Davis, L. J. M.; Ellis, B. L.; Ramesh, T. N.; Nazar, L. F.; Bain, A. D.; Goward, G. R.  $^6\text{Li}$  1D EXSY NMR Spectroscopy: A New Tool for Studying Lithium Dynamics in Paramagnetic Materials Applied to Monoclinic  $\text{Li}_2\text{VPO}_4\text{F}$ . *J. Phys. Chem. C* **2011**, *115*, 22603–22608.

(35) Davis, L. J. M.; He, X. J.; Bain, A. D.; Goward, G. R. Studies of Lithium Ion Dynamics in Paramagnetic Cathode Materials using  $^6\text{Li}$  1D Selective Inversion Methods. *Solid State Nucl. Magn. Reson.* **2012**, *42*, 26–32.

(36) La Mar, G. N.; Horrocks, W. DeW.; Holm, R. H. *NMR of Paramagnetic Molecules*; Academic Press Inc.: New York, 1973.

(37) Brown, I. D.; Shannon, R. D. Empirical Bond-Strength-Bond-Length Curves for Oxides. *Acta Crystallogr.* **1973**, *29*, 266–282.

(38) Brown, I. D. Bond Valence as an Aid to Understanding the Stereochemistry of O and F Complexes of Sn(II), Sb(III), Te(IV), I(V) and Xe(VI). *J. Solid State Chem.* **1974**, *11*, 214–233.

(39) Gonzalez-Platas, J.; Gonzalez-Silgo, C.; Ruiz-Perez, C. VALMAP2.0: Contour Maps using the Bond-Valence-Sum Model. *J. Appl. Crystallogr.* **1999**, *32*, 341–344.

(40) Bain, A. D.; Fletcher, D. A. Selective-Inversion Experiments Applied to Chemical Exchange in Coupled Spin Systems. *Mol. Phys.* **1998**, *95*, 1091–1098.

(41) Bain, A. D. Chemical Exchange in NMR. *Prog. Nucl. Magn. Reson. Spectrosc.* **2003**, *43*, 63–103.

(42) Bauer, C.; Freeman, R.; Frenkiel, T.; Keeler, J.; Shaka, A. Gaussian Pulses. *J. Magn. Reson.* **1984**, *58*, 442–457.

(43) Forsen, S.; Hoffman, R. Study of Moderately Rapid Chemical Exchange Reactions by Means of Nuclear Magnetic Double Resonance. *J. Chem. Phys.* **1963**, *39*, 2892–2901.

(44) Forsen, S.; Hoffman, R. Exchange Rates by Nuclear Magnetic Multiple Resonance. III. Exchange Reactions in Systems with Several Nonequivalent Sites. *J. Chem. Phys.* **1964**, *40*, 1189–1196.

(45) Brown, I. D. Bond Valences—A Simple Structural Model for Inorganic Chemistry. *Chem. Soc. Rev.* **1978**, *7*, 359–376.

(46) Islam, M. S.; Driscoll, D. J.; Fisher, C. A. J.; Slater, P. R. Atomic-Scale Investigation of Defects, Dopants, and Lithium Transport in the  $\text{LiFePO}_4$  Olivine-Type Battery Material. *Chem. Mater.* **2005**, *17*, 5085–5092.

(47) Grey, C. P.; Dupre, N. NMR Studies of Cathode Materials for Lithium-Ion Rechargeable Batteries. *Chem. Rev.* **2004**, *104*, 4493–4512.

(48) Middlemiss, D. S.; Illott, A. J.; Clement, R. J.; Strobridge, F. C.; Grey, C. P. Density Functional Theory-Based Bond Pathway Decompositions of Hyperfine Shifts: Equipping Solid-State NMR to Characterize Atomic Environments in Paramagnetic Materials. *Chem. Mater.* **2013**, *25*, 1723–1734.